

Kimi, K.B., et al., 2024, Deformation of the Gruithuisen region lava tube under compressional stress on the Moon: *Geology*, v. XX, p. XXX–XXX, <https://doi.org/10.1130/G52143.1>

Supplemental Material

Additional descriptions of the procedure followed in the study, supporting figures, tables, and links to model GIFs of lunar lava tube deformation.

GSA SUPPLEMENTARY

Deformation of the Gruithuisen Region Lava Tube under Compressional Stress on the Moon

K.B. Kimi^{1,2*}, Harish³, K.S. Sharini⁴, Anil Chavan¹, and S. Vijayan¹

¹*Physical Research Laboratory, Navrangpura, Ahmedabad 380009, Gujarat, India*

²*Indian Institute of Technology, Palaj, Gandhinagar 382055, Gujarat, India*

³*Laboratory for Atmospheric and Space Physics, University of Colorado, Boulder, Colorado
22 80303, USA*

⁴*Department of Earth Sciences University of Western Ontario, London, ON N6A 3K7,
Canada*

I. Measurements:

In this study, we used Lunar Reconnaissance Orbiter (LRO)-Narrow Angle Camera (NAC) images with resolutions ranging from ~1 to 1.5 meters per pixel (**Robinson *et al.*, 2010**), LRO NAC DTM (Digital Terrain Model) (**Henriksen *et al.*, 2017**), and a merged Lunar Orbiter Laser Altimeter (LOLA) and Selenological and Engineering Explorer (SELENE)-Terrain Camera (TC) digital elevation model (DEM) with spatial resolution ~59 m/pixel and vertical resolution ~3–4 m (SLDEM2015) (**Barker *et al.*, 2016**) for detailed mapping and topography analysis. Additionally, we incorporated shapefiles of previously identified wrinkle ridges for cross-referencing and validation (**Thompson *et al.*, 2017**). We used an orthographic projection in the mapping process. The length of the wrinkle ridges and the major and minor axes of the collapsed pits were measured in ArcGIS (Table S3&S5). Collapsed pit depths were estimated by computing the difference between contour values (5 m interval) of collapsed edges and floors (Table S5). Similarly, the heights of raised features

were determined from the difference in contour values (5 m interval) between the highest contour of the raised feature and the surrounding floor (Table S6).

II. Estimation of Strain, Stress, and Force:

We estimated the normal strain in the study area using the largest wrinkle ridge present in the study area (Fig S1). We employed the same method previously utilized in the works of **Watters and Robinson, 1997 and Watters, 2022**. The strain is the result of how the geological structure responds to external forces. The formula for calculating normal strain, ϵ , involves:

$$\epsilon = \frac{\Delta L}{L_0} \dots \dots \dots Eq1$$

where, ΔL is the change in length, and L_0 is the original length.

A systematic approach was taken to evaluate normal strain (ϵ): Ten horizontal point-to-point, straight-line distances across the large wrinkle ridge were measured, providing a comprehensive sampling. Then, the cross-length sections were calculated across these ten sections of the wrinkle ridge (Fig S1). Then, we estimated the difference between the cross-length and the horizontal straight-line distance, representing the length change (ΔL). The horizontal straight-line distance represented the original length (L_0). By using these two measured parameters, we calculated the normal strain (ϵ) (Table S4). Then, normal stress (σ) was calculated:

$$\sigma = E * \epsilon \dots \dots \dots Eq2$$

where, E is Elastic Modulus, and ϵ is normal strain.

The force (F) was then calculated by:

$$F = \sigma * A \dots \dots \dots Eq3$$

where, σ is normal stress, and A is the area of geometry of the model.

III. 3D Modelling in Ansys:

In our study, both the geometries and the mesh were designed to ensure that computer simulations could be carried out with a significant reduction in computation time while still maintaining the precision of the results. Our model simplifies complex scenarios for better understanding. It is important to note that the 3D simulation results in this study primarily emphasize the structural changes when subjected to force rather than providing precise quantification. The quantification is challenging since accurately simulating the actual conditions may not be feasible. Therefore, this model focuses on visualizing and understanding the shapes (geometries) that emerge under the compressional stress of a tube.

Static structural analysis

After specifying the material properties (Table S2) and constructing the geometry (Fig S2), we applied boundary conditions in the static structural analysis based on the observed orientation of wrinkle ridges and the force calculated from the largest wrinkle ridge within the study area. In this setup, an external force was applied in the negative x-direction (from East to West), and it was counterbalanced by fixed supports at the opposite end (West) (details already discussed in the manuscript methodology section). So, based on applied boundary conditions, the governing equations solved by Ansys software in linear static analysis is:

$$\{F\} = [K]\{u\} \dots \dots \dots Eq4$$

where, F is the applied external force, [K] is the stiffness matrix, and u is the displacement.

Eigenbuckling analysis

After completing the static structural analysis, an eigenbuckling analysis was performed to determine the load at which the structure is expected to undergo buckling. This calculation was carried out in the Ansys software using the following equation:

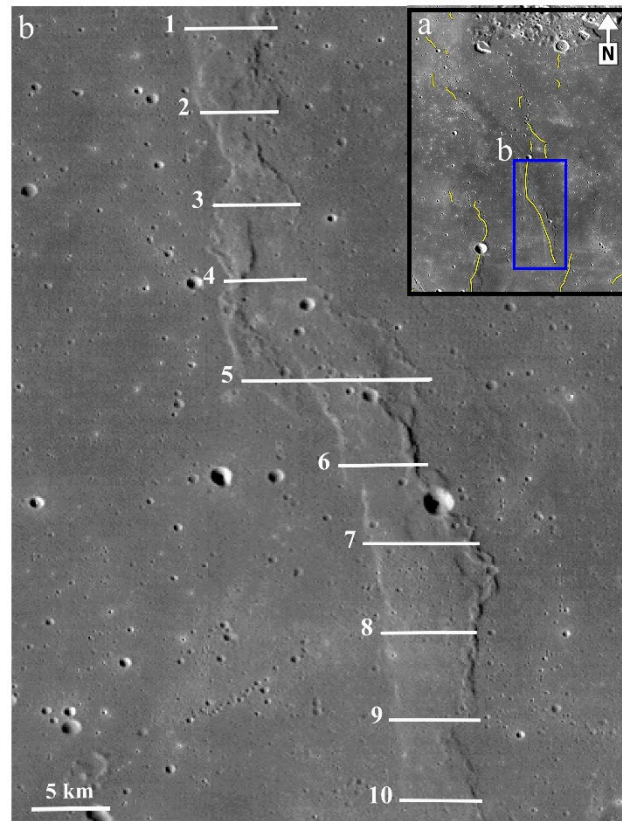
$$[K + \lambda_n[S]]\{\Psi_n\} = 0 \dots \dots \dots Eq5$$

where, [K] is the stiffness matrix, and [S] is the stress stiffness matrix.

The outcome of this analysis is the load multiplier (λ_n) and the mode shape (ψ_n), whose values are provided in Table S7 and whose mode shapes GIFs are in Figs S14-S33. We have attached the model's GIFs that illustrate the total deformation mode shape. Total deformation represents the cumulative displacement experienced by the structure in the x, y, and z directions due to external forces.

In total, twenty mode shapes/3D models were studied, and some of these 3D models shared similarities: Model 2 resembles Model 1 (Figs S15 & S14); Model 4 resembles Models 3, 8, and 10 (Figs S17, S16, S21 & S23); Model 7 resembles Models 5, 9, and 11 (Figs S20, S18, S22 & S24); and Model 18 is similar to Model 19 (Figs S31 & S32). Among the similar models, the most likely match model was chosen for comparison with the observation.

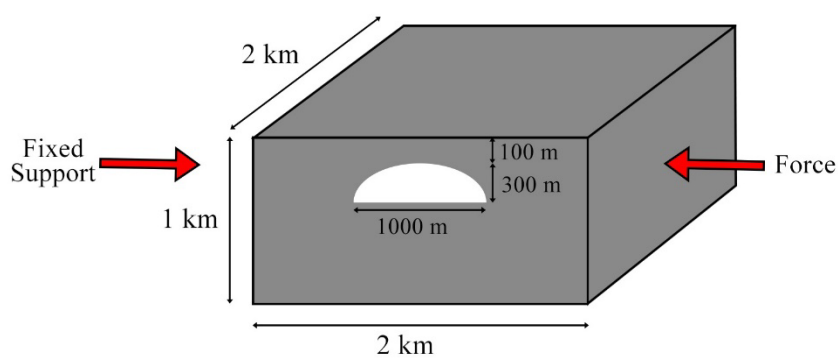
85 **Supplementary Figures:**



86

87 **Fig S1:** Measured ten cross-sections across the large wrinkle ridge in the study area.

88



89

90 **Fig S2:** The dimensions of 2 km x 2 km x 1 km were employed in the 3D model, and a semi-
 91 elliptical hollow section of a 1 km width, one-third height, and a 100 m thick roof was used.
 92 These geometries were designed to ensure that computer simulations could be carried out
 93 with a significant reduction in computation time. Note that dimensions are not for scale. The
 94 red arrow indicates the direction of the applied fixed support/boundary condition and the
 95 force applied in the opposite direction.

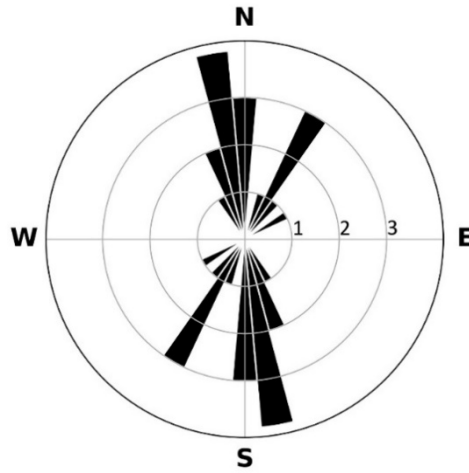


Fig S3: Orientations of the wrinkle ridges. Please refer to Figure 1b for the wrinkle ridges used for plotting the rose diagram.

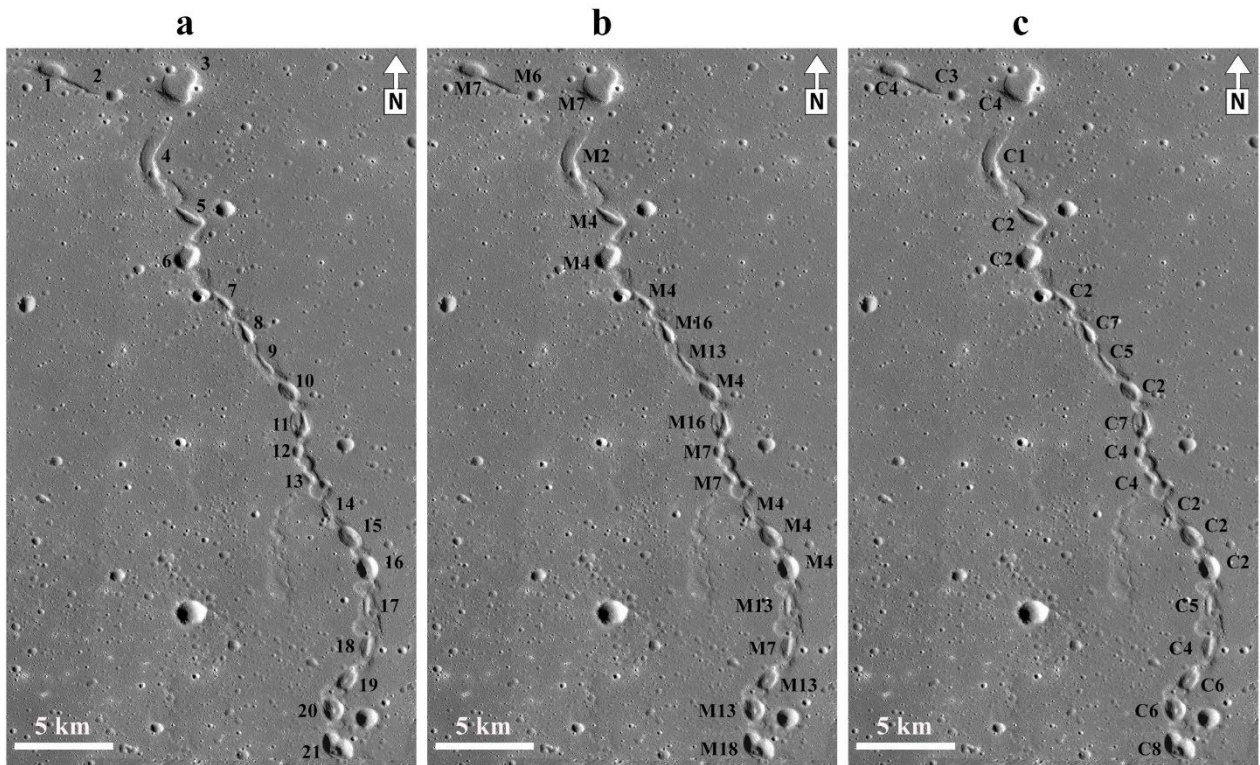
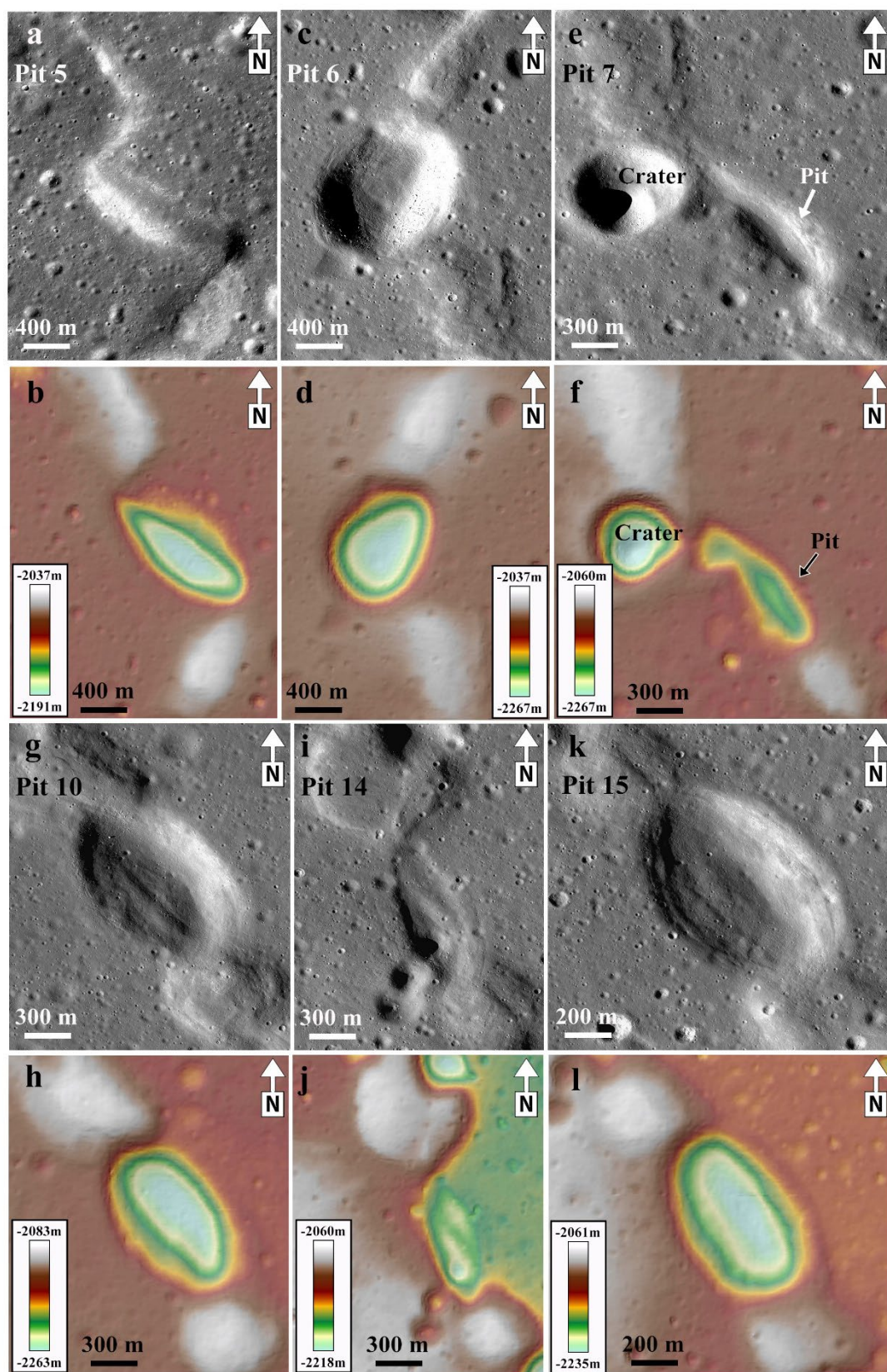
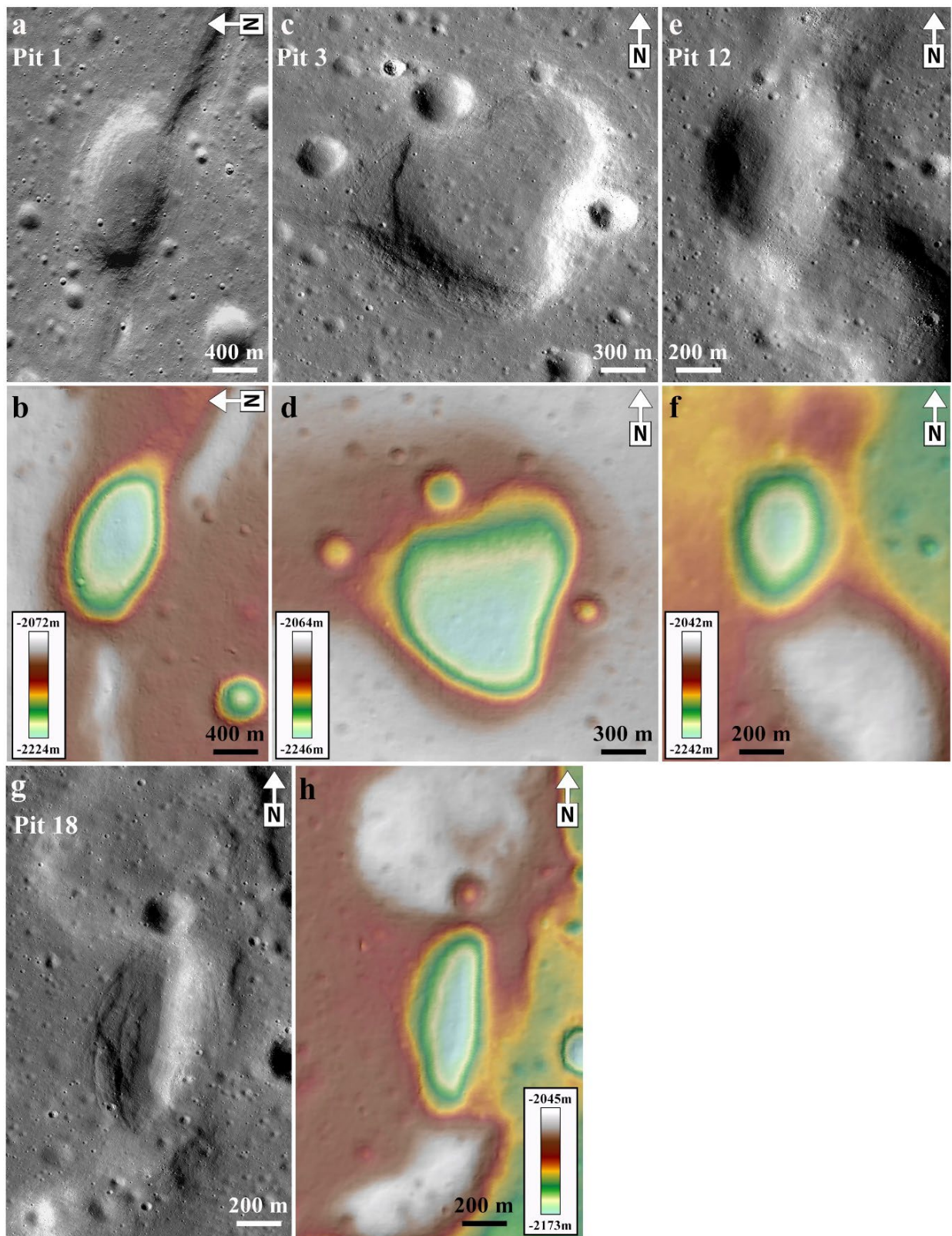


Fig S4: a) Pits number and locations. b) The model aligned with the pits and associated raised features. Capital M stands for model. c) The type/characteristics of the pits and associated raised features. Capital C stands for type/characteristic. An explanation of the types can be found in the manuscript.



103 **Fig S5:** Pits 5, 6, 7, 10, 14, and 15 with alternating collapsed and raised shown in LROC-
 104 NAC images and NAC DTM.



105

106 **Fig S6:** Pits 1, 3, 12, and 18 have partially collapsed pits and raised features shown in LROC-
 107 NAC images and NAC DTM.

108

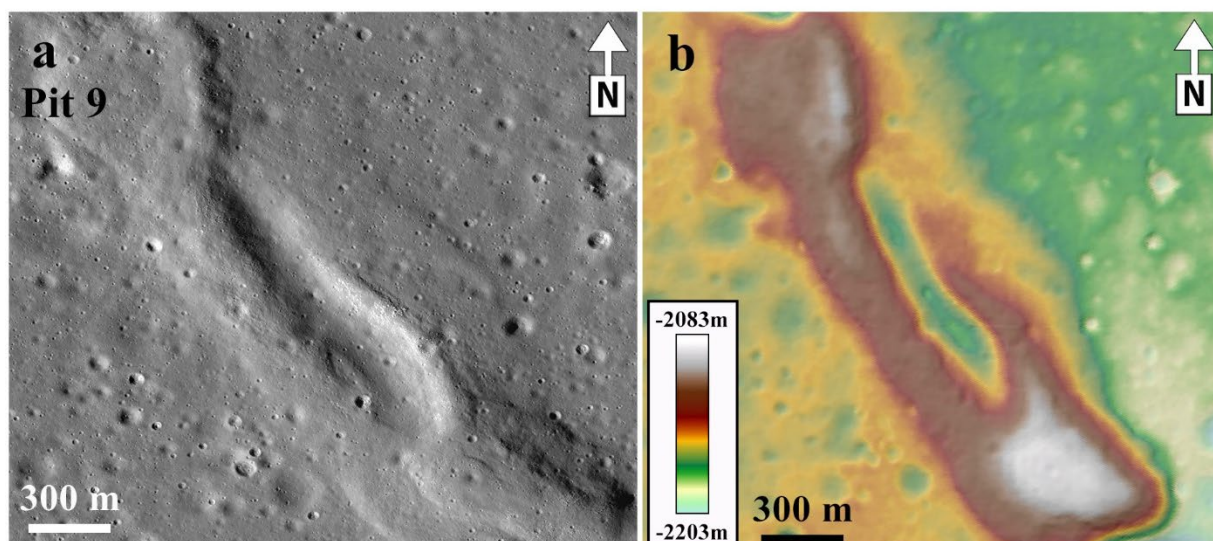


Fig S7: Collapsed pit 9 surrounded by raised features shown in LROC-NAC images and NAC DTM.

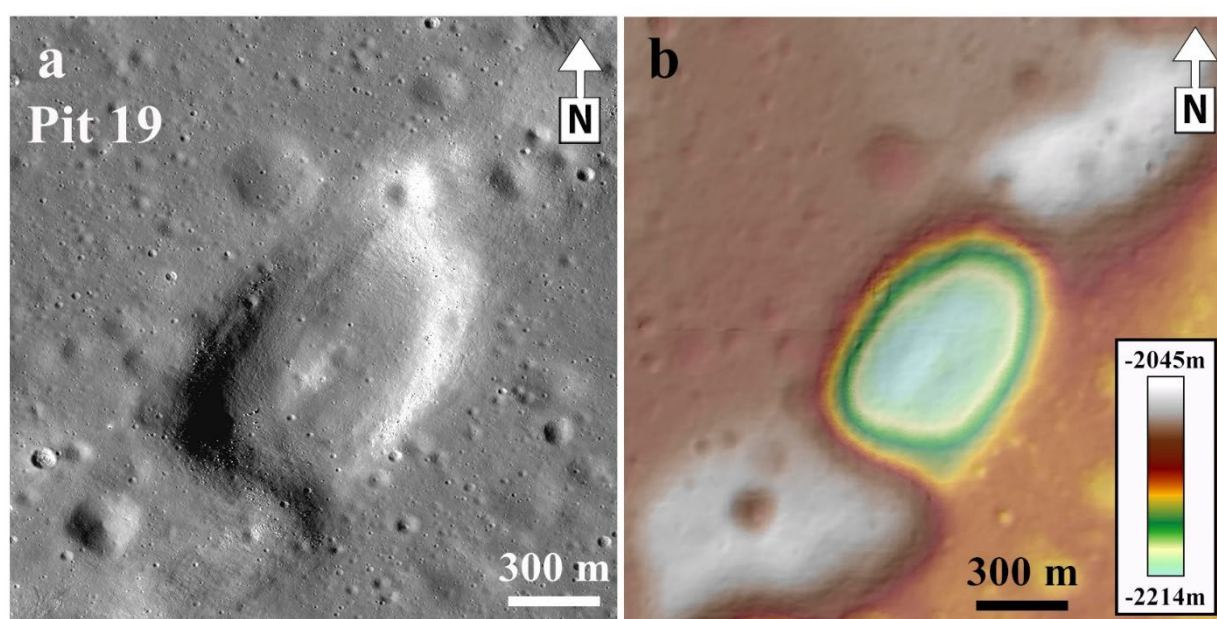


Fig S8: Collapsed pit 19 with raised features at the centre shown in LROC-NAC images and NAC DTM.

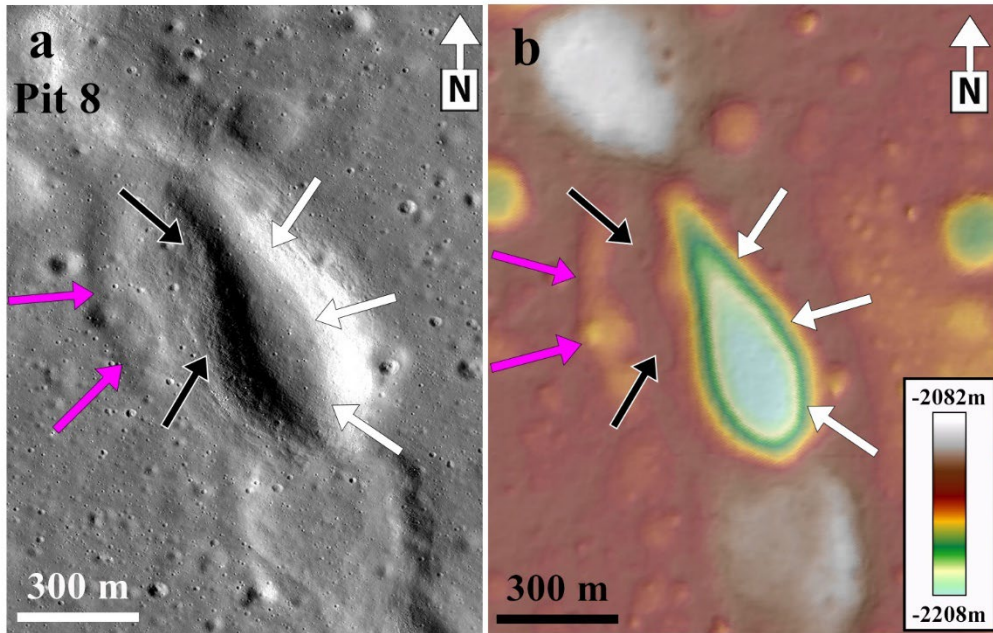


Fig S9: Collapsed pit 8, with one side exhibiting a more pronounced collapse (white arrows) than the other half (pink arrows) shown in LROC-NAC images and NAC DTM.

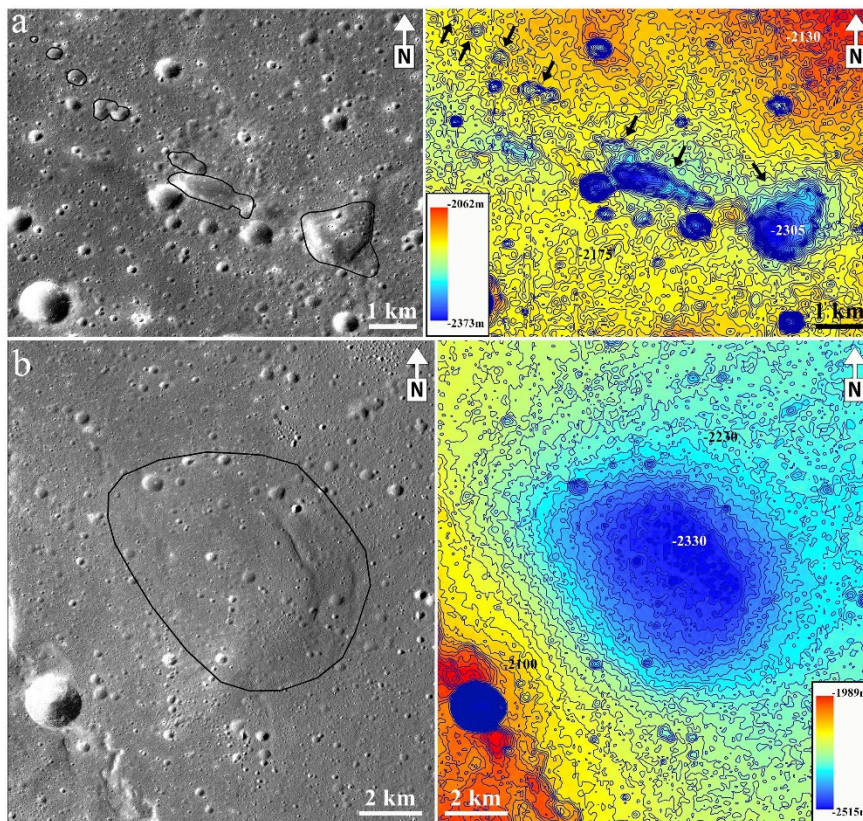
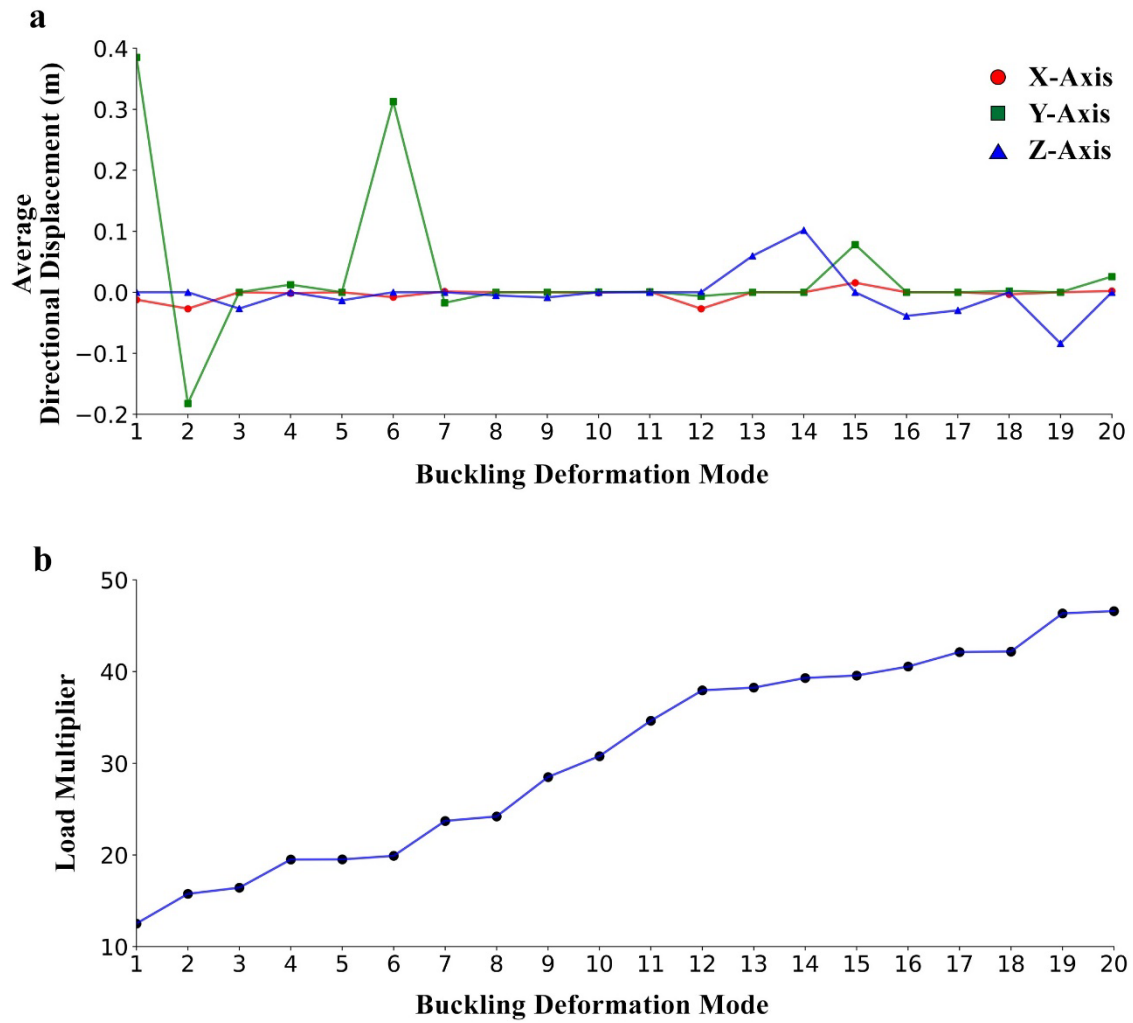


Fig S10: a) Collapsed chain 2 with seven collapsed pits marked in black polygons, and b) Isolated collapsed pit marked in black polygon shown in LROC-NAC images and SLDEM2015.



122

123 **Fig S11:** a) Displays the average directional displacement versus mode shape for twenty
 124 simulated models, illustrating variations in displacement magnitude and direction. Negative
 125 displacement signifies movement along the negative x, y, and z axes. b) Load multiplier
 126 versus mode shape, indicating the amount of load that needs to be multiplied by the estimated
 127 force ($1.4 \times 10^{14} \text{N}$) to achieve the depicted mode shape.
 128

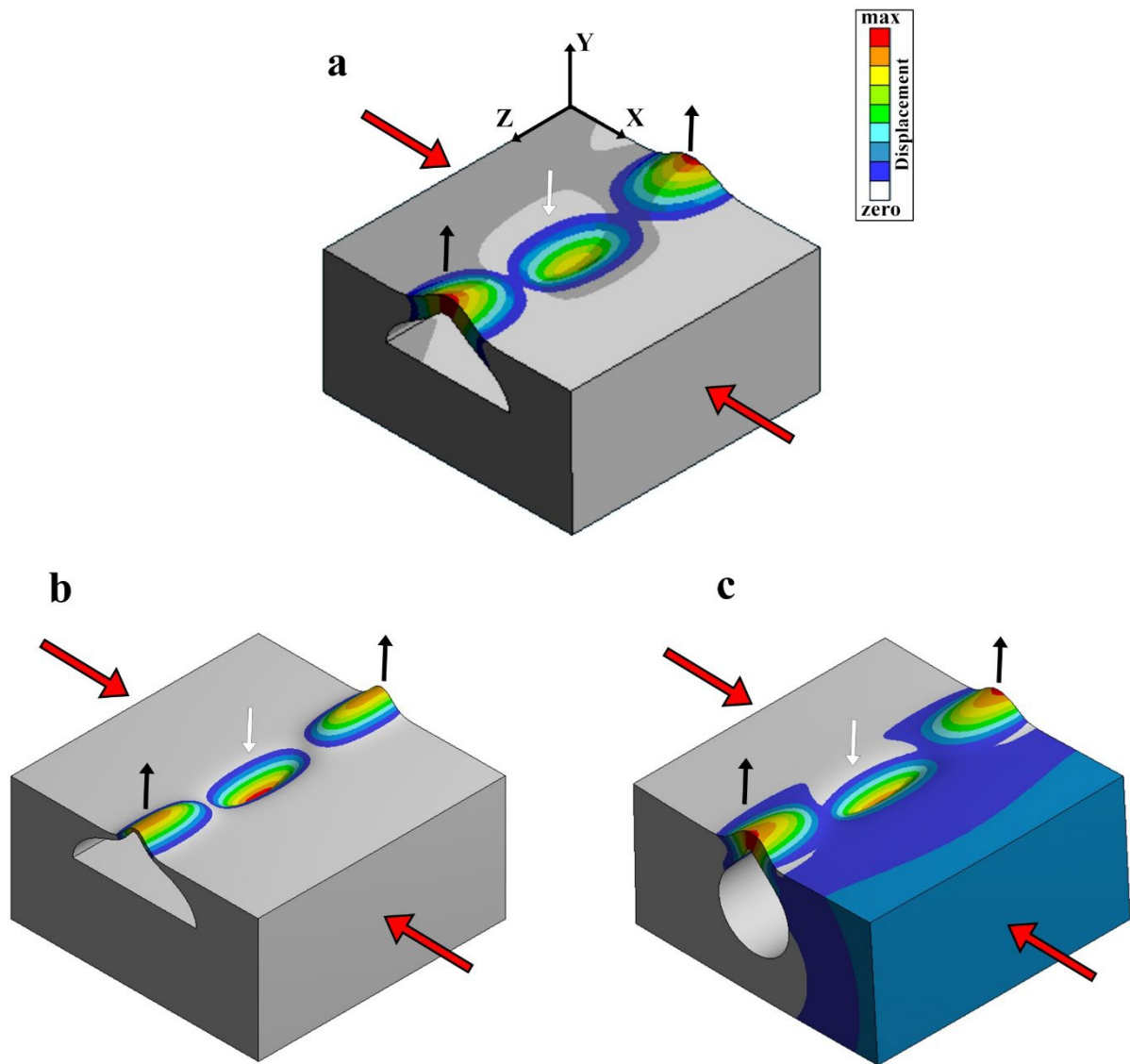
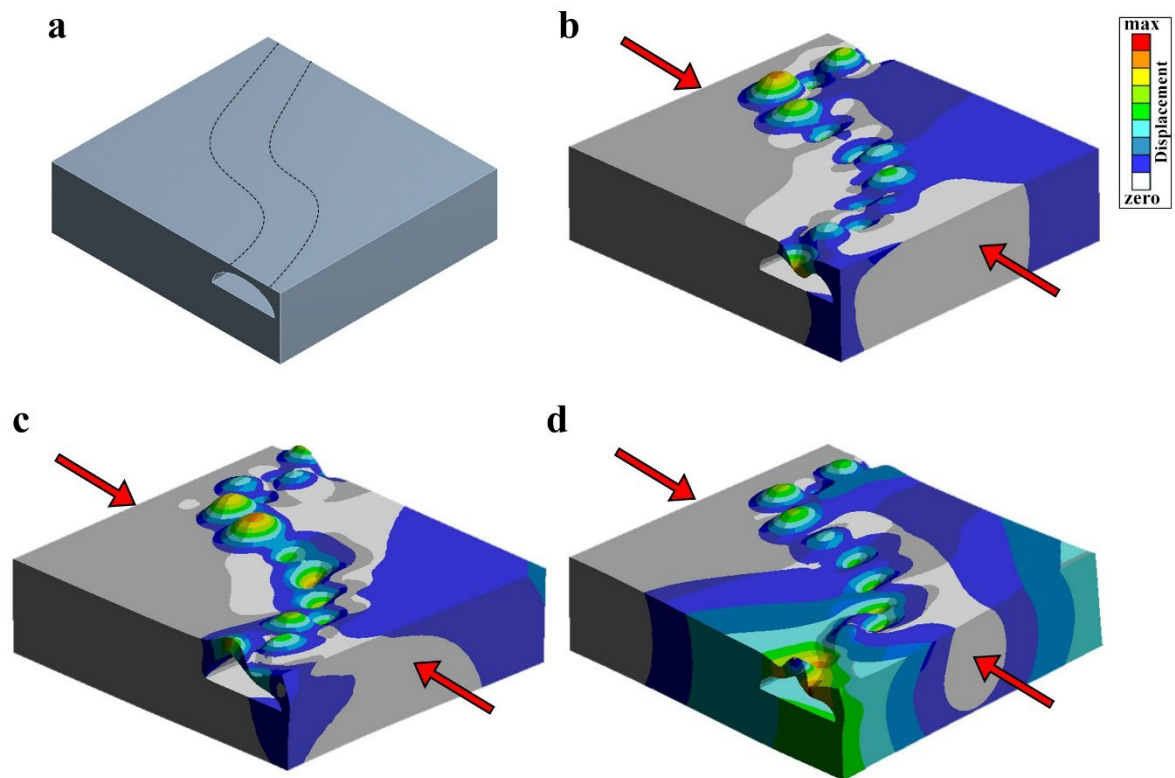


Fig S12: Comparison of models in response to changes in lava tube roof thickness and tube cross-section compared to the model used in the study. All models have dimensions of 2X2X1 km³. a) The original model of the study with a lava roof thickness of 100m and a semi-elliptical cross-section. b) The model with a reduced lava roof thickness of 20m shows a similar deformation pattern to the original model. However, the deformation occurred at a smaller load multiplier, and the features became narrow, indicating that collapse may occur earlier than in the original model. The roof thickness of 20 m over 1000 m wide is unstable and will collapse due to gravity (Theinat *et al.*, 2020). The goal of this model is to assess sensitivity to thickness. c) The Model maintaining a 100m lava roof thickness with a circular tube shape also has similar deformation, but deformation occurred at a higher load multiplier and showed narrow features. Here, we considered the simplest tube cross-section, which is circular, for simplicity. However, it can vary to more complex shapes (For details on the cross-section, please refer to (Chwała, et al., 2024)). The GIFs of models can be found at <https://doi.org/10.5281/zenodo.11075944>



145

146 **Fig S13:** a) An illustration of a simple curved lava tube with dimensions identical to the
 147 straight lava tube within 3500mX3700mX1000m (lXbXh) block. b-d) Highlights different
 148 deformation patterns in the curved lava tube, which incorporates deformation features
 149 observed in the straight tube. The GIFs of models can be found at
 150 <https://doi.org/10.5281/zenodo.11075944>

151 **Supplementary Tables:**

152

153

Table S1: NAC ids utilized in this study.		
NAC ID	Incident Angle	Resolution
	°	m/pixel
M181459858LE	68	1.5
M181459858RE	68	1.5
M190888252LE	55	1.5
M190888252RE	55	1.5
M1119179101LE	38	1.4
M1119179101RE	38	1.4
M1152158374LE	53	1.4
M1152158374RE	53	1.4
M1185115900LE	74	1.3
M1185115900RE	74	1.3
M1234553109LE	70	1.3
M1333294118LE	52	1.0
M1333294118RE	52	1.0
M1333301164LE	53	1.0

Table S2: Material properties information.	
Parameter (Unit)	Value
Young's Modulus (GPa)	30
Poisson's ratio	0.3

Table S3: Wrinkle ridges length and Azimuth information.						
No	Length	Start_lon	End_lon	Start_lat	End_lat	Azimuth
	km	km	km	km	km	°
1	7.61	-1297.43	-1297.50	1069.00	1061.38	0.48
2	4.26	-1298.86	-1297.56	1054.86	1050.80	-17.81
3	2.01	-1359.07	-1358.00	1062.42	1064.42	28.05
4	2.18	-1346.83	-1350.76	1067.82	1065.97	64.71
5	1.90	-1341.94	-1343.26	1068.31	1066.30	33.14
6	5.72	-1359.74	-1358.39	1071.17	1065.63	-13.72
7	4.82	-1335.69	-1339.78	1067.31	1062.16	38.41
8	9.14	-1365.60	-1365.43	1059.80	1050.35	-1.04
9	15.07	-1360.19	-1351.41	1050.51	1037.30	-33.62
10	4.91	-1270.62	-1273.06	1023.94	1018.57	24.43
11	14.55	-1317.46	-1324.71	1045.70	1030.62	25.70
12	7.84	-1312.95	-1313.52	1022.77	1014.56	3.94
13	57.37	-1314.63	-1300.55	1011.10	955.17	-14.12
14	26.56	-1343.28	-1338.98	992.72	966.41	-9.29
15	6.27	-1357.06	-1355.26	993.84	987.75	-16.39
16	7.57	-1273.14	-1271.43	1032.86	1025.43	-13.00

154

Table S4: Details of the strain and stress values estimated from the wrinkle ridge.								
No.	Fig	Lat	Lon	Cross Length (Lt)	Horizontal Length (Lo)	Change Length (ΔL)	Strain (ϵ)	Stress (σ)
	No	°	°	km	km	km		GPa
1	S1	33.287	-43.409	5.209	5.197	0.012	2.37E-03	7.12E-02
2		33.101	-43.389	4.401	4.392	0.009	2.05E-03	6.14E-02
3		32.898	-43.354	4.938	4.932	0.006	1.29E-03	3.86E-02
4		32.732	-43.334	4.630	4.610	0.020	4.23E-03	1.27E-01
5		32.509	-43.177	10.630	10.615	0.015	1.37E-03	4.12E-02
6		32.324	-43.072	5.037	5.017	0.020	3.97E-03	1.19E-01
7		32.151	-42.989	6.525	6.509	0.016	2.51E-03	7.53E-02
8		31.956	-42.973	5.500	5.482	0.018	3.32E-03	9.95E-02
9		31.765	-42.959	5.217	5.211	0.006	1.18E-03	3.55E-02
10		31.585	-42.944	4.571	4.568	0.003	7.23E-04	2.17E-02

Table S5: Details on 29 collapsed pits.										
Pit No	NAC ID	Model No	Figure No	Lat	Lon	Major axis km	Minor axis km	Ellipticity	Depth	Descriptions
				°	°	km	km		m	
Pit Chain 1										
1	M1234553109LE	7	S6a&b	35.27	-43.91	1.05	0.78	0.26	100	Partially collapsed and raised features
2	M1234553109LE, M181459858LE	6	2g&h	35.25	-43.81	2.42	1.46	0.39	35	Collapsed with one side displaying a steeper slope
3	M181459858LE	7	S6c&d	35.24	-43.67	1.70	1.60	0.06	150	Partially collapsed and raised features
4	M181459858LE	2	2a&b	35.11	-43.73	3.73	0.38	0.90	45	Channel shape collapsed
5	M181459858LE	4	S5a&b	35.00	-43.65	1.42	0.62	0.57	90	Alternating collapsed and raised features
6	M181459858LE	4	S5c&d	34.92	-43.66	1.16	0.99	0.15	155	Alternating collapsed and raised features
7	M181459858LE	4	S5e&f	34.84	-43.59	0.93	0.28	0.70	55	Alternating collapsed and raised features
8	M181459858LE	16	S9a&b	34.78	-43.56	1.45	0.49	0.66	70	One side exhibiting a more pronounced collapse
9	M181459858RE	13	S7a&b	34.72	-43.52	1.38	0.16	0.88	30	Collapsed surrounded by raised features
10	M181459858RE	4	S5g&h	34.67	-43.47	1.35	0.58	0.57	110	Alternating collapsed and raised features
11	M181459858RE	16	4a&b	34.61	-43.45	1.59	0.56	0.65	115	One side exhibiting a more pronounced collapse
12	M181459858RE	7	S6e&f	34.56	-43.46	0.73	0.38	0.48	65	Partially collapsed and raised features
13	M181459858RE	7	3a&b	34.51	-43.44	0.67	0.28	0.58	45	Partially collapsed and raised features
14	M181459858RE	4	S5i&j	34.45	-43.40	1.31	0.26	0.80	60	Alternating collapsed and raised features
15	M181459858RE	4	S5k&l	34.40	-43.36	1.31	0.60	0.54	95	Alternating collapsed and raised features
16	M181459858RE	4	2d&e	34.35	-43.33	1.43	0.55	0.62	160	Alternating collapsed and raised features
17	M181459858RE	13	3d&e	34.28	-43.33	1.22	0.17	0.86	30	Collapsed surrounded by raised features
18	M181459858RE	7	S6g&h	34.20	-43.33	1.16	0.37	0.68	65	Partially collapsed and raised features
19	M181459858RE	13	S8a&b	34.14	-43.37	0.94	0.71	0.25	105	Collapsed with a mound
20	M181459858RE	13	3g&h	34.08	-43.39	1.40	0.51	0.64	130	Collapsed with a mound
21	M190888252RE	18	4d&e	34.01	-43.39	1.69	0.95	0.44	225	Two fused collapsed

Table S5: Details on 29 collapsed pits.

Table S5: Details on 29 collapsed pits.									
Pit No	NAC ID	Model No	Figure No	Lat	Lon	Major axis	Minor axis	Ellipticity	Depth
				°	°	km	km		m
Pit Chain 2									
22	M1152158374RE, M1152158374LE	-	S10a	33.89	-43.55	1.81	1.56	0.13	100
23		-		33.93	-43.67	1.57	0.63	0.60	80
24		-		33.96	-43.70	0.83	0.40	0.51	15
25		-		34.01	-43.77	0.69	0.49	0.29	25
26		-		34.04	-43.80	0.42	0.29	0.31	20
27		-		34.07	-43.82	0.31	0.22	0.30	20
28		-		34.08	-43.84	0.14	0.11	0.19	5
Isolated pit									
29	M1333294118LE, M1185115900RE	-	S10b	32.42	-42.74	8.26	4.28	0.48	110
Potential Eruptive vent									
-	M1119179101LE, M1119179101RE	-	1b	35.33	-44.19	-	-	-	610

Table S6: Raised feature details.					
Raised No	Lat °	Lon °	Raised Elevation m	Floor Elevation m	Height m
1	35.04	-43.69	-2045	-2080	35
2	34.96	-43.64	-2040	-2090	50
3	34.89	-43.63	-2065	-2110	45
4	34.81	-43.57	-2090	-2145	55
5	34.72	-43.52	-2085	-2125	40
6	34.65	-43.45	-2090	-2130	40
7	34.53	-43.43	-2045	-2115	70
8	34.43	-43.38	-2065	-2110	45
9	34.37	-43.34	-2080	-2130	50
10	34.25	-43.33	-2050	-2100	50
11	34.11	-43.39	-2060	-2100	40
12	34.05	-43.38	-2070	-2110	40
13	33.70	-43.16	-2075	-2160	85

Table S7: Results obtained from the 3D simulated model. Please refer to the attached Excel sheet.

References

- Barker, M.K. *et al.* (2016) ‘A new lunar digital elevation model from the Lunar Orbiter Laser Altimeter and SELENE Terrain Camera’, *Icarus*, 273, pp. 346–355.
- Chwała, M., Komatsu, G. and Haruyama, J. (2024) ‘Structural stability of lunar lava tubes with consideration of variable cross-section geometry’, *Icarus*, 411, p. 115928.
- Henriksen, M.R. *et al.* (2017) ‘Extracting accurate and precise topography from LROC narrow angle camera stereo observations’, *Icarus*, 283, pp. 122–137.
- Robinson, M.S. *et al.* (2010) ‘Lunar Reconnaissance Orbiter Camera (LROC) Instrument Overview’, *Space Science Reviews*, 150(1), pp. 81–124. Available at: <https://doi.org/10.1007/s11214-010-9634-2>.
- Theinat, A.K. *et al.* (2020) ‘Lunar lava tubes: Morphology to structural stability’, *Icarus*, 338, p. 113442. Available at: <https://doi.org/10.1016/j.icarus.2019.113442>.
- Thompson, T.J. *et al.* (2017) ‘Global lunar wrinkle ridge identification and analysis’, in *48th Annual Lunar and Planetary Science Conference. 48th Annual Lunar and Planetary Science Conference*, p. 2665.
- Watters, T.R. (2022) ‘Lunar Wrinkle Ridges and the Evolution of the Nearside Lithosphere’, *Journal of Geophysical Research: Planets*, 127(3), p. e2021JE007058. Available at: <https://doi.org/10.1029/2021JE007058>.

181 Watters, T.R. and Robinson, M.S. (1997) 'Radar and photoclinometric studies of wrinkle
182 ridges on Mars', *Journal of Geophysical Research: Planets*, 102(E5), pp. 10889–10903.
183 Available at: <https://doi.org/10.1029/97JE00411>.
184